Review in Advance first posted online on January 4, 2013. (Changes may still occur before final publication online and in print.)

Charge Transport at the Metal-Organic Interface

Shaowei Chen,[1] Zhenhuan Zhao,[2] and Hong Liu[2,3]

[1]Department of Chemistry and Biochemistry, University of California, Santa Cruz, California 95064; email: shaowei@ucsc.edu

[2]State Key Laboratory of Crystal Materials, Center of Bio and Micro/Nano Functional Materials, Shandong University, Jinan, Shandong 250100, China; email: hongliu@sdu.edu.cn

[3]Beijing Institute of Nanoenergy and Nanosystems, Chinese Academy of Sciences, Beijing 100085, China

Annu. Rev. Phys. Chem. 2013. 64:221–45

The *Annual Review of Physical Chemistry* is online at physchem.annualreviews.org

This article's doi:
10.1146/annurev-physchem-040412-110035

Keywords

metal-ligand contacts, molecular junctions, organically capped nanoparticles, intraparticle charge delocalization

Abstract

This review focuses on the impacts of metal-organic interfacial bonding interactions on the charge-transport dynamics involved in molecular junctions as well as organically capped nanoparticles. Whereas mercapto derivatives have been used extensively as the ligands of choice to functionalize metal and nanoparticle surfaces with the formation of metal-thiolate interfacial bonds, recent studies show that metal-carbon covalent linkages may be fabricated by the deliberate design and selection of functional moieties. With enhanced electronic interactions between metals and organic ligands, the interfacial contact resistance diminishes drastically, leading to the emergence of unprecedented optical and electronic properties of the junctions and nanoparticles. These mechanistic insights are of fundamental significance in the development of molecule- and nanoparticle-based electronic devices, in particular, in light of the diverse metal-nonmetal bonding interactions that have been extensively observed in organometallic chemistry.

1. INTRODUCTION

Resonant tunneling: in electron tunneling through a double barrier, resonances occur at a certain electron energy at which the transmission coefficient is equal to 1

Electronic circuits based on simple molecules or nanostructures represent an effective and attractive solution to the grand challenge of continuing diminishment of feature size with ever-enhanced performance, a concept pioneered by Aviram & Ratner (1). Within such a framework, simple organic molecules or nanostructures (e.g., nanoparticles, nanotubes, nanowires) serve as the active components to achieve the diverse functionalities of circuit elements in manipulating electrical outputs, analogous to silicon-based semiconductor materials, by taking advantage of the ready manipulation of their structures and properties through molecular design and nanoscale engineering. In these devices, the circuit elements are generally in contact with a metal lead, with the interfacial contact possibly playing a critical role in determining device performance. For instance, in molecular electronics represented by a nanojunction bridged by a thin film of organic molecules, it is well known that the junction conductance can be manipulated not only by the chemical backbones of the organic molecules but also by the metal-molecule bonding contacts and molecule-molecule interactions (2–6). In these, depending on the terminal structures and hence the metal-molecule hybridization, the interfacial contact may exhibit ohmic behaviors or may behave as a Schottky barrier for charge transfer (7–10).

Such a variation of the metal-organic bonding interactions and hence interfacial contact resistance is also anticipated to impact the charge-transfer properties of organically capped transition-metal nanoparticles (11–16). Whereas a number of studies have been carried out both at the single-particle level and with particle ensembles (17–26), most are focused on mercapto derivatives as the ligands of choice for nanoparticle surface functionalization because of the strong affinity of thiol groups to metal surfaces. Recently a series of studies demonstrated that other metal-organic bonding linkages can be readily produced. This not only affects the growth dynamics of the nanoparticles (27), but more interestingly also controls the spilling of core electrons into the organic matrix and hence the energetic barrier for interparticle and intraparticle charge transfer (vide infra). One can see that understanding such nanoscale electron transfer is fundamentally significant in the use of nanoparticles as structural units in the fabrication of new functional nanodevices.

Whereas the structural configurations may differ drastically between the molecular junctions and the nanoparticles, both exhibit a clearly defined metal-organic interface, and there is a significant overlap of the fundamental mechanisms that govern the interfacial electron transfer. Thus in this review article we summarize some of the latest progress in the investigation of metal-ligand interfacial contacts on the charge-transfer characteristics in two systems (nanojunctions and nanoparticles) and then highlight some emerging challenges and possible future directions.

2. MOLECULAR JUNCTIONS

The simplest form of a nanojunction consists of two metal electrode leads that are positioned with a nanoscale gap and bridged by a single organic molecule or a thin film of organic materials (6). The junction is typically decomposed into three individual barriers through the molecular body and metal-molecule contacts on both sides of the molecules, and the metal-molecule contacts are generally separated from the molecular body (28), when the applied bias is much lower than the HOMO (highest occupied molecular orbital)-LUMO (lowest unoccupied molecular orbital) gap of the molecule and the junction barrier height, and nonresonant tunneling is the main mechanism of charge transport.

There are several leading approaches to the preparation of nanojunction electrodes. The first involves so-called break junctions, in which a nanogap is produced by breaking a metal wire through mechanical pulling, chemical etching, or electromigration (29, 30–35). The second entails

controlled etching of a metal thin film by, for instance, electron-beam lithography (36). Once a gap is formed, organic molecules can then be assembled between the metal leads forming a nanojunction. The third approach involves the deposition (or self-assembly) of an organic thin film onto a metal substrate before the introduction of a second conducting lead, which may be a metal thin film by vapor deposition, a conventional electrode, or a conducting scanning probe (6, 37, 38). In such a configuration, depending on the dimensions of the second lead electrode, one can evaluate the charge transport of a single molecule or an ensemble.

Schottky contacts: exhibit rectified charge transport with a barrier (>kT) defined by the metal Fermi energy and the semiconductor band edge

Regardless of the preparation methods of the molecular junctions, the chemical nature of the interfacial contacts between the metal electrodes and the organic molecules/layers has been found to significantly impact the charge transport across nanojunctions (6). Schottky contacts on wide-band-gap materials often exhibit significant device-to-device variations and nonideal behaviors in current-voltage (I-V) measurements, whereas with ohmic contacts at the interface, charge transport across the junctions is facilitated.

In an early study, Lindsay and coworkers (39) developed a reliable technique to measure the conductivity properties of single molecules in which they inserted molecules of 1,8-octanedithiol into a 1-octanethiol self-assembled monolayer (SAM) on an Au(111) surface by a replacement reaction. The low concentration of the dithiol molecules made it possible to isolate one from another and hence to examine the transport properties at the single-molecule level. Gold colloidal nanoparticles were then anchored onto the terminal thiols, and a junction was created by using a gold-coated conducting atomic force microscope (AFM) tip to locate and contact the gold nanoparticles (**Figure 1*a***). As highlighted by the I-V curves in **Figure 1**, transport measurements showed that the junction conductance varied statistically as multiples of a fundamental curve ascribed to assemblies in which a single dithiol molecule linked the gold nanoparticle to the underlying gold substrate. From these studies, the resistance of a single octanedithiol molecule was estimated to be 900 $\pm$ 50 MΩ—for comparison, the electrical resistance of a single α,α'-xylyldithiol (XYL) molecule was estimated to be ~18 $\pm$ 12 MΩ, based on coulomb staircase studies of gold nanoparticles immobilized onto the XYL dithiol self-assembled monolayer surfaces (25). Additionally, the junction conductance through bonded contacts was at least four orders of magnitude greater than that of nonbonded contacts (i.e., through the methyl terminus), along with a different voltage dependence.

In another study, Engelkes et al. (40) prepared nanoscale tunnel junctions by contacting gold-, platinum-, or silver-coated AFM tips to SAMs of alkanethiol or alkanedithiol molecules on polycrystalline gold, platinum, or silver substrates (**Figure 2**). For alkanedithiol monolayers (**Figure 3*b***), the sigmoidal I-V profiles exhibited symmetrical characters, suggesting similar bonding contacts at both molecular termini, whereas for alkanethiol monolayers (**Figure 3*a***), slightly more currents were observed when the tip was biased negatively relative to the substrate. Importantly, the I-V curves can be fitted by the Simmons equation for tunneling through a square barrier,

$$I = \frac{qA}{4\pi^2\hbar s^2}\left\{\left(\phi - \frac{qV}{2}\right)\cdot\exp\left(-\frac{2s\sqrt{2m}}{\hbar}\sqrt{\theta - \frac{qV}{2}}\right) - \left(\phi + \frac{qV}{2}\right)\cdot\exp\left(-\frac{2s\sqrt{2m}}{\hbar}\sqrt{\theta + \frac{qV}{2}}\right)\right\} \quad (1)$$

where A is the junction area, s is the width of the barrier, m is the electron mass, and ϕ is the barrier height (41). At low biases, the equation can be simplified as

$$R = R_0 \exp(\beta n) \quad (2)$$

where R is the junction resistance (V/I), R_0 is the effective contact resistance, β is the structure-dependent attenuation factor, and n is the number of repeat units of the alkyl spacer. According

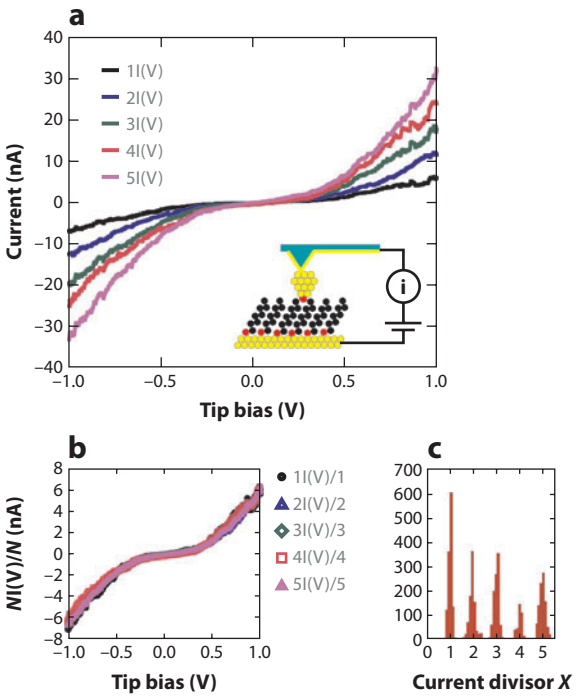

Figure 1

(*a*, *inset*) Schematic representation of the experiment. The sulfur atoms (*red dots*) of octanethiols bind to a sheet of gold atoms (*yellow dots*), and the octyl chains (*black dots*) form a monolayer. The second sulfur atom of a 1,8-octanedithiol molecule inserted into the monolayer binds to a gold nanoparticle, which in turn is contacted by the gold tip of the conducting atomic force microscope (AFM). Illustrated in the main panel are I(V) curves measured with the apparatus diagrammed in the inset. The five curves shown are representative of distinct families, *N*I(V), that are integer multiples of a fundamental curve, $I(V)$ ($N = 1, 2, 3, 4,$ and 5). (*b*) Curves from panel *a* divided by 1, 2, 3, 4, and 5. (*c*) Histogram of values of a divisor, X (a continuous parameter), chosen to minimize the variance between any one curve and the fundamental curve, $I(V)$. It is sharply peaked at integer values 1.00 ± 0.07 (1,256 curves), 2.00 ± 0.14 (932 curves), 3.00 ± 0.10 (1,002 curves), 4.00 ± 0.10 (396 curves), and 5.00 ± 0.13 (993 curves). (Spreads are ± 1 standard deviation.) Of 4,579 randomly chosen curves, over 25% correspond to the $X = 1$ (single-molecule) peak. No obvious correlation was noted between particle size and the number of molecules contacted. Conducting AFM data were acquired with a PicoSPM microscope (Molecular Imaging) using silicon cantilevers (spring constant, 0.35 N m^{-1}) sputter-coated with 5 nm of chromium followed by 50 nm of gold. Imaging was done under toluene in a nitrogen atmosphere. Figure reproduced by permission from Reference 39, copyright (2001) American Association for the Advancement of Science.

to Simmons' theory, the tunneling coefficient (β) is correlated to the height of the energy barrier at zero bias ($\frac{4\pi\alpha}{h}\sqrt{2m\theta}$), with α a numerical parameter for extending the model with a rectangular barrier to that with a nonrectangular one, or to account for the effective mass of electrons (42–45). **Figure 4** depicts the semilog plots of the variation of the junction resistance with the alkyl chain length, which exhibit a clear exponential correlation. From linear regression of the experimental data, R_0 and β can be quantitatively evaluated from the intercept and slope, respectively. There are at least three aspects that warrant attention here. First, the β coefficients are the same for both the alkanethiol and alkanedithiol monolayers, suggesting the same scaling of the film thickness with chain length. Second, the contact resistance is one to two orders of magnitude lower with the doubly bound alkanedithiol junctions than with the singly bound alkanethiol ones. Third,

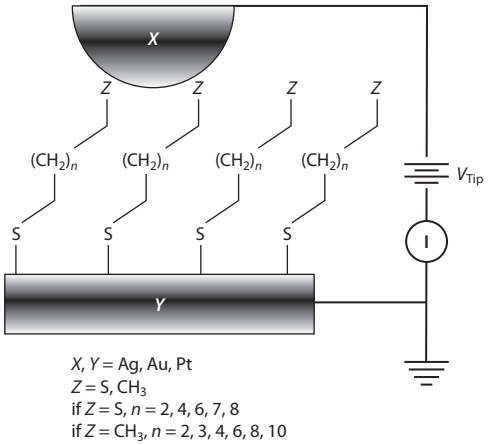

Figure 2

Schematic representation of a molecular tunnel junction formed using conductive-probe atomic force microscopy (AFM). A metal-coated (gold, silver, or platinum) AFM tip is brought into contact with a self-assembled monolayer of alkanethiols or alkanedithiols of various lengths on a gold-, silver-, or platinum-coated silicon substrate. Voltage is swept at the tip, and the resulting current is measured. Figure reproduced with permission from Reference 40, copyright (2004) American Chemical Society.

the contact resistance decreases with increasing work function of the metal electrodes, Ag < Au < Pt, as shown in **Figure 5**, which is accounted for by hole transport across the junction as the Fermi level is nearer the HOMO* than the LUMO*.

The impacts of interfacial contacts on charge transport have also been observed in molecular junctions with macroscopic electrodes. For instance, Slowinski and coworkers (46) employed two mercury electrodes to examine the tunneling resistance of monolayers and bilayers of *n*-alkanethiols. There are two junction configurations: one with the two mercury electrodes modified with a SAM of alkanethiols and the other with the alkanethiol monolayers adsorbed only on one mercury electrode. The authors then brought the two electrodes into contact,

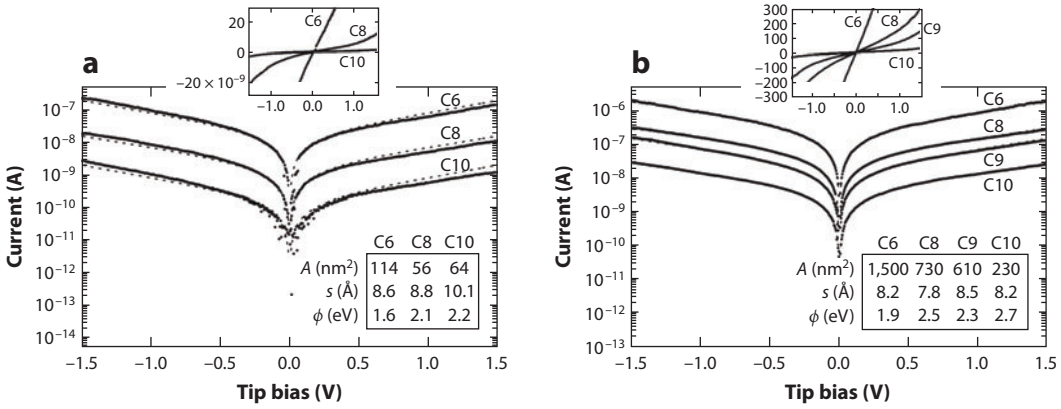

Figure 3

Representative semilog plot of I-V traces of C6, C8, and C10 Au-alkanethiol-Au (*a*) and Au-alkanedithiol-Au (*b*) junctions. The absolute value of the current is displayed. Dashed lines are fits to Equation 1. (*Insets*) Sigmoidal I-V behavior on linear axes. Figure reproduced with permission from Reference 40, copyright (2004) American Chemical Society.

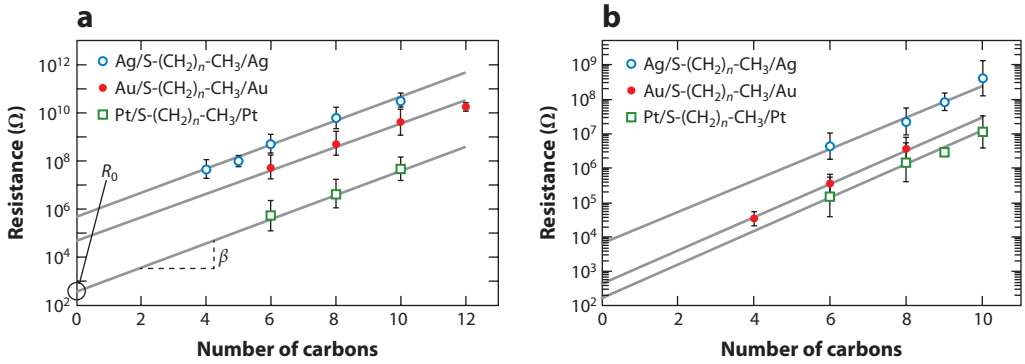

Figure 4

Resistance versus length plots for alkanethiol (*a*) and alkanedithiol (*b*) junctions. Data points are average resistance values of approximately 10 experiments performed with different tips. Lines are not least-squares fits to the data but are defined by the average R_0 and β values for the same set of tips. Figure reproduced with permission from Reference 40, copyright (2004) American Chemical Society.

forming a macroscopic junction, with a structure of Hg-S-$(CH_2)_n$-CH_3 | CH_3-$(CH_2)_n$-S-Hg and Hg-S-$(CH_2)_m$-CH_3 | Hg, respectively. For both monolayer and bilayer junctions, the tunneling currents decreased exponentially with the junction width defined by the monolayer/bilayer thickness, and a tunneling coefficient $\beta = 1/CH_2$. Yet the tunneling current of the monolayer junctions was at least an order of magnitude smaller than that of the bilayer junctions containing the same number of carbon atoms across the junction. For instance, the authors reported that the tunneling current recorded for a monolayer of *n*-octadecanethiol was approximately 2.0 ± 0.5-fold smaller than that for a bilayer of *n*-nonanethiol, although the geometric thickness of the latter junction was greater than that of the former. This was accounted for by the inefficient electronic coupling at the -CH_3 | Hg interface as compared with that at the -CH_3 | CH_3- interface, although both were nonbonding in nature (47).

Further enhancement of the junction charge transport can be achieved by covalent linking at the interface between the two SAMs (in bilayer junctions). This was highlighted by Whitesides and coworkers (48), who prepared two types of bilayer junctions (**Figure 6**). The first (**Figure 6*b***) involves SAMs of simple *n*-alkanethiols on a mercury electrode and on another metal electrode

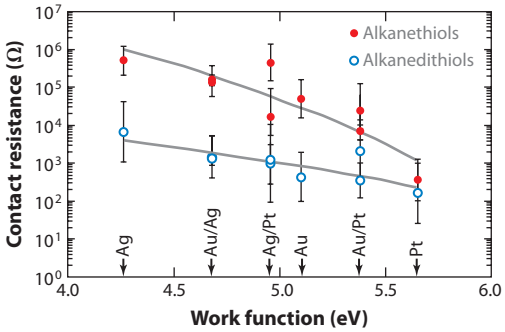

Figure 5

Contact resistance (R_0) as a function of electrode metal work function for junctions comprising alkanethiols (*filled circles*) and alkanedithiols (*open circles*). The solid lines are guides for the eye. Figure reproduced with permission from Reference 40, copyright (2004) American Chemical Society.

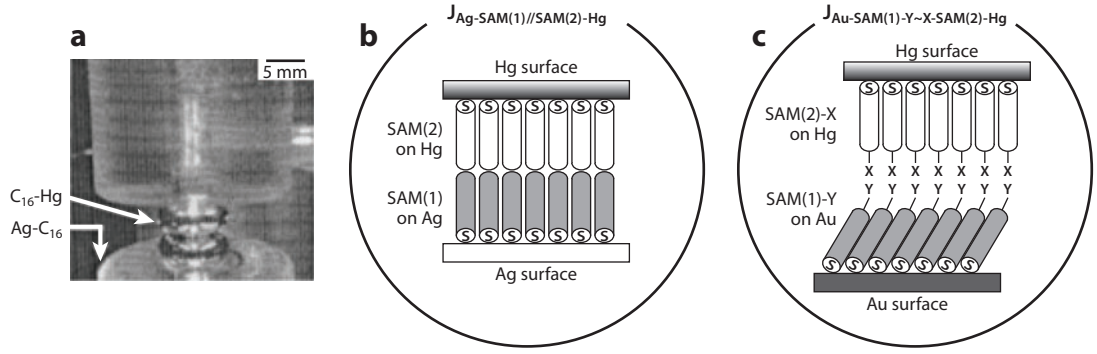

Figure 6

Schematic illustrations of junctions with structures $J_{Ag-SAM(1)//SAM(2)-Hg}$ and $J_{Au-SAM(1)-X\sim Y-SAM(2)-Hg}$. (*a*) Photograph of a $J_{Ag-C16//C16-Hg}$ junction. The scale bar represents ~0.5 mm. (*b*) A self-assembled monolayer (SAM) on the surface of a thin evaporated film of silver in the assembly of $J_{Ag-SAM(1)//SAM(2)-Hg}$ junctions. (In this case, M = Ag, as silver gives highly ordered SAMs.) This electrode was covered with a solution of hexadecane containing 1-mM thiol. A small drop of mercury (5 μL) was expressed into a solution of hexadecanethiol (HDT) from a capillary connected to a mercury reservoir, and a SAM of HDT was allowed to form on it. The HDT-covered mercury drop (C_{16}-Hg) was then brought into contact with the solid electrode using a micromanipulator. The area of interfacial contact was estimated using a microscope. With each electrode connected to an electrometer (in two-electrode mode), a potential was applied and the response recorded, and then the potential increased in steps over a range of voltages to generate I-V curves. (*c*) Junctions of the structure $J_{Au-SAM(1)-X\sim Y-SAM(2)-Hg}$ created as described for $J_{Ag-SAM(1)//SAM(2)-Hg}$ except that one electrode was a thin film of gold, and the thiols used had terminal groups that could react and form covalent bonds (X = carboxylic anhydride, Y = H_2N) or interact strongly but noncovalently (X = CO_2H and Y = HO_2C, or X = CO_2H and Y = H_2N) through hydrogen or ionic bonds. Figure reproduced with permission from Reference 48, copyright (2001) John Wiley and Sons.

(e.g., gold and silver). The contact between the two monolayers was van der Waals in nature with a -CH_3 | CH_3- interface. The second configuration (**Figure 6*c***) entails covalent, hydrogen, or ionic bonds that bridge the monolayer interfaces through specific functional groups at the monolayer terminals. In comparison with the first junction, the tunneling currents of the second type of junctions were markedly enhanced (**Figure 7**). For instance, the current with a hydrogen-bonding interface afforded by -COOH | NH_2- and -COOH | HOOC- showed a 9- and 40-fold increase, respectively. More interestingly, for a covalently linked interface in which the two monolayers were connected with an amide bond [-C(O)NH-], the junction charge transport displayed an enhancement by three to four orders of magnitude. Based on these measurements, the authors estimated that the resistance of the -CH_3 | CH_3- interface for charge transport was equivalent to that of an alkyl spacer of six σ bonds, -$(CH_2)_6$-.

In the above studies, the organic molecules are assembled onto the electrode surface largely by metal-thiolate bonds. In fact, mercapto derivatives have been used as the molecules of choice in the formation of stable molecular assemblies on metal surfaces by virtue of the strong affinity of thiol moieties to transition metals (49). However, recent studies demonstrate that with an interfacial contact of metal-carbon covalent bonds, the interfacial contact resistance may be reduced markedly, leading to further improvement of the junction charge transport. For instance, Cheng et al. (50) used trimethyl tin ($SnMe_3$)-terminated polymethylene chains to form single-molecule junctions with a break junction technique (**Figure 8**). Au-C bonds were formed by the displacement of the $SnMe_3$ moieties by gold atoms at the electrode surface. The resulting junctions showed a conductance that was ~100 times larger than that with analogous alkanes with most other terminations (e.g., -NH_2), which was ascribed to the formation of Au-C σ bonds. Studies with a variation of the alkane chain length showed that the junction tunneling currents decreased exponentially with molecular length, with a decay constant (β) of 0.97 per CH_2 (46), suggesting a nonresonant

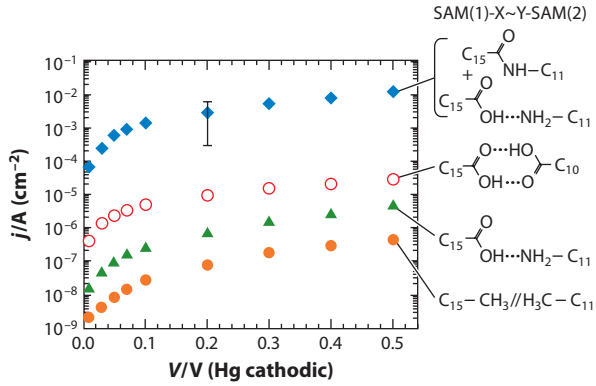

Figure 7

Plots of current density as a function of the bias voltage between mercury and gold electrodes for junctions Au-SAM(1)-X~Y-SAM(7)-Hg. The error bar is plus or minus the standard deviation of the data. The symbols X and Y denote terminal functional groups of the monolayers, the double lines represent a van der Waals contact, the three middle dots are for hydrogen bonding, and the single line is for covalent bonding. Figure reproduced with permission from Reference 48, copyright (2001) John Wiley and Sons.

transport mechanism, similar to conventional junctions based on metal-thiolate linkages (49).

Using the same junction configuration, further studies with π-conjugated molecules demonstrated enhanced electronic coupling between the metal electrode and the π system (**Figure 9**) (51). For instance, the junctions formed with the prototypical example of 1,4-dimethylenebenzene showed a conductance approaching one conductance quantum ($G_0 = 2e^2/h$), and for longer oligophenyl-based junctions, the charge transport was tunneling in nature. Furthermore, calculations based on density functional theory (DFT) showed that for the Au-xylene-Au junction, near-resonant transmission was likely, with a crossover to tunneling for the longer oligomers.

Furthermore, using junctions with organic molecules sandwiched between a mercury electrode and highly doped silicon, Yaffe et al. (52) found that the substitution of an alkyl monolayer with an alkenyl one on the Si(111) surface further facilitated the junction charge transport, with the double bonds enhancing the coupling between the organic monolayers and the silicon substrate. In fact, theoretical studies based on DFT showed that the silicon-related states extended further into the molecular region in the alkenyl ligands (up to the third carbon) than in the alkyl case (up to the second carbon). Experimentally, this was manifested by an increase of the junction current density at a given bias as a result of the increasing contact conductance, i.e., $(4.7 \pm 1.3) \times 10^{-7}$ G_0 for alkyl and $(13 \pm 8) \times 10^{-7}$ G_0 for alkenyl monolayers.

The examples cited above clearly demonstrate that interfacial resistance may be reduced significantly by switching nonbonding contacts with bonding ones, and of the interfacial bonding interactions, metal-carbon covalent bonds are more effective in electronic coupling between the molecules and the electrode than metal-thiolate bonds. Furthermore, the hybridization state of the anchoring carbon is critical in manipulating the interfacial electronic coupling and hence the charge transport of a molecular junction. In fact, metal-carbon bonding interactions have been recognized to impact charge-transport characteristics in nanoelectronic devices based on carbon nanotubes or graphene, in which metal leads are generally deposited onto the carbon nanostructures to make electrical contacts (53). A series of theoretical studies (54–56) demonstrated that in addition to metal work functions, the chemical nature of the interfacial bonding interactions also plays a significant role in determining the height of the Schottky barrier.

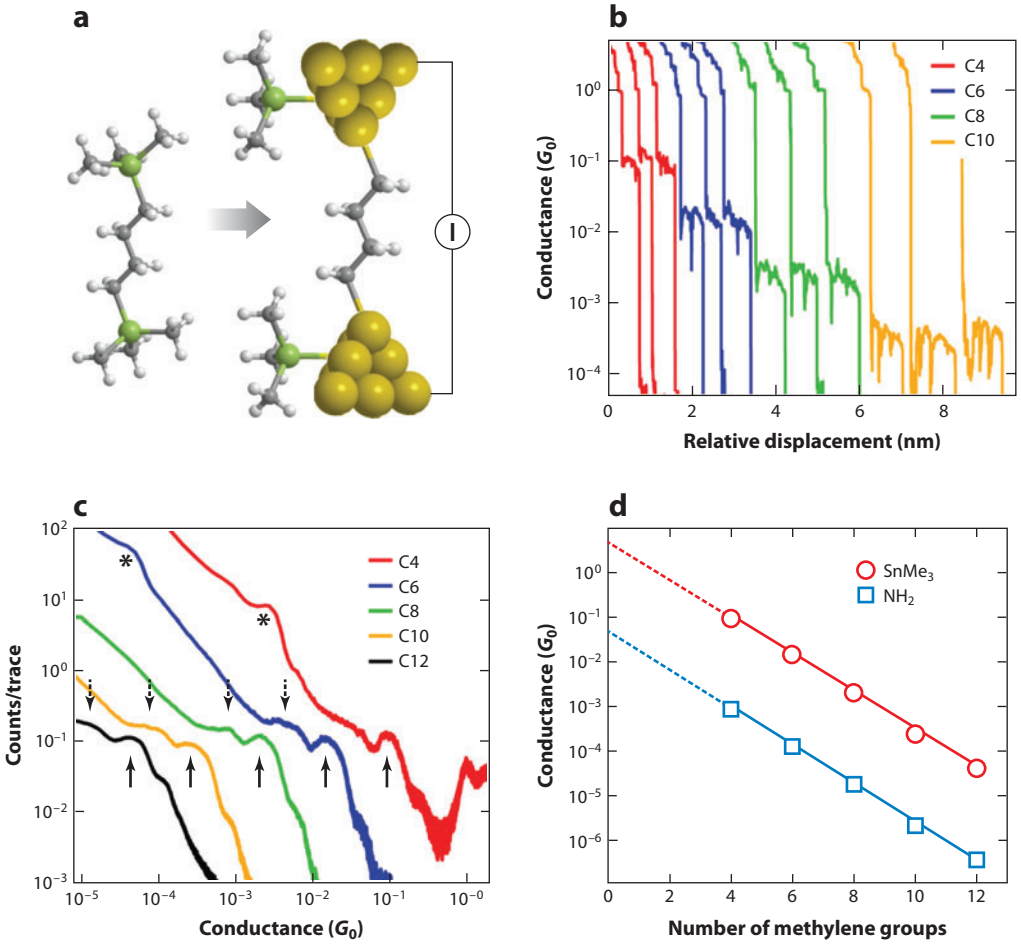

Figure 8

Conductance data for $SnMe_3$-linked alkanes. (*a*) Junction formation and conductance measurements with 1,4-*bis*(trimethylstannyl)butane molecules between gold electrodes. Hydrogen atoms are shown in white, carbon atoms in gray, and tin atoms in green. (*b*) Sample traces showing conductance on a logarithmic scale versus relative displacement for $SnMe_3$-terminated alkanes with four (C4, *red*), six (C6, *blue*), eight (C8, *green*), and ten (C10, *orange*) methylene groups in the backbone. (*c*) Conductance histograms for C4, C6, C8, C10, and C12. Each histogram is constructed from 10,000 traces and is generated without any data selection. Bin size is $10^{-4}G_0$ for C4, $10^{-5}G_0$ for C6 and C8, $10^{-6}G_0$ for C10, and $10^{-7}G_0$ for C12. Upward arrows indicate primary conductance peaks; downward arrows indicate lower conducting shoulders. Asterisks indicate conductance peaks due to the dimer molecule formed in situ. (*d*) Conductance at the peak on a logarithmic scale versus the number of methylene groups in the backbone for $SnMe_3$-terminated alkanes (*red*) and diamine-terminated alkanes (*blue*). Figure reproduced with permission from Reference 50, copyright (2011) Nature Publishing.

These fundamental insights may account for the wide disparity of the contact resistance between carbon nanotubes and metal leads. For instance, an ohmic contact between silver and amorphous carbon nanotubes was observed with arrays of one-dimensional heterostructures fabricated by combining electrochemical deposition and chemical vapor deposition with porous membranes as the templates (57). Nihei and coworkers (58) grew multiwall carbon nanotubes with a nickel catalyst layer on a titanium electrode surface by hot-filament chemical vapor deposition and found that the contact resistance with the nickel/titanium electrode was two orders of magnitude lower

Ohmic contact: a nonrectifying junction with a linear and symmetrical current-potential profile

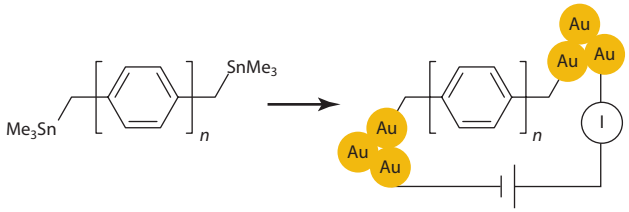

P1, $n = 1$; P2, $n = 2$; P3, $n = 3$; P4, $n = 4$

Figure 9

In situ formation of direct Au-electrode-C bonds starting from $SnMe_3$ precursors. Figure reproduced with permission from Reference 51, copyright (2011) American Chemical Society.

than that without the titanium substrate. This was ascribed to the formation of titanium carbide during nanotube growth and the end bonding configuration of the nanotubes on titanium. In a study based on the first-principles quantum mechanical density functional and matrix Green's function methods, Matsuda et al. (59) examined the I-V characteristics and contact resistance of end- and side-contacted metal-carbon nanotube and metal-graphene interfaces with five different metals (titanium, palladium, platinum, copper, and gold). They observed that in the end-contacted configuration, the contact resistance (normalized to surface carbon atoms) was 107 kΩ for titanium, 142 kΩ for palladium, 149 kΩ for platinum, 253 kΩ for copper, and 187 kΩ for gold, whereas in the side-contacted configuration, it was markedly higher, at 8.6 MΩ for palladium, 34.7 MΩ for platinum, and 630 MΩ for copper.

These results strongly suggest that end contact between a carbon nanotube or graphene and a metal is most effective in reducing the interfacial contact resistance, likely a result of the formation of more extensive chemical bonding at the interface. In addition, among the metals investigated, palladium appears to be the optimal choice in wetting carbon nanotubes and graphene, leading to an improved diminishment of the contact resistance (60–63). This is consistent with results observed with metal nanoparticles passivated by metal-carbon covalent bonds, as detailed below. However, the nature of the interfacial bonds (e.g., single bonds, double bonds) involving carbon nanotubes or graphene has remained largely unresolved in experimental measurements. Breakthroughs toward this end are urgently needed so that the performance of nanoelectronic devices based on these carbon nanostructures may be further improved and optimized (64).

3. ORGANICALLY CAPPED NANOPARTICLES

That direct bonding interactions between metals and carbon nanotubes lead to a drastic decrease in the interfacial contact resistance may be exploited for the manipulation of nanoparticle optical and electronic properties by passivating the nanoparticles with metal-carbon covalent bonds. This has been demonstrated recently in a series of studies. In this section, we highlight some recent progress in the functionalization of metal nanoparticles with metal-carbon covalent bonds and the impacts of these unique interfacial bonding interactions on nanoparticle charge-transfer chemistry in comparison with the metal-thiolate ones.

4.1. Metal-Carbon Bonds

In most earlier studies, alkanethiols and other thiol derivatives were used extensively as the ligands of choice to stabilize metal nanoparticles by taking advantage of the strong affinity of thiol groups to transition-metal surfaces (65–69). Yet because of the lack of interesting chemistry of

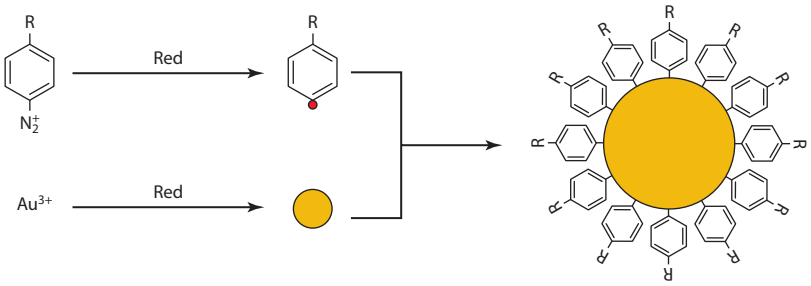

Figure 10

Schematic of the synthesis of metal nanoparticles passivated by metal-carbon covalent bonds. Figure reproduced with permission from Reference 75, copyright (2006) American Chemical Society.

the metal-sulfur bonds, the impacts of the metal-ligand interfacial bonding interactions on the nanoparticle material properties have been largely ignored. For instance, in studies of nanoparticle electronic conductivity, the predominant energetic barrier to interparticle charge transport is generally assumed to result from the organic capping ligands that intercalate between adjacent particles (70–73). Yet with the variation of the metal leads as well as that of the chemical structure of the molecular linkers (including metal-anchoring groups), one may envision that the energetic landscape for charge transport will be readily manipulated. For instance, diazonium derivatives have been used rather extensively for the functional grafting of a variety of transition-metal surfaces by virtue of the formation of a metal-carbon covalent bond. Theoretical studies based on DFT calculations (74) have shown that the energy for the chemisorption of aryl moieties onto metal surfaces (e.g., titanium, iron, copper, silver, palladium, and gold) by diazonium precursors decreases from left to right in the periodic table with the increasing number of d electrons. They correlated this changing trend with the center of the metal d band, which shifts further below the Fermi level with an increasing number of d electrons, thus effectively weakening the bonding between the metal surfaces and the aryl adsorbates. Importantly, this study also suggests that the adsorbates may adopt two surface configurations: an upright orientation in favor of a metal-carbon σ bond, which is anticipated with transition metals to the right of iron in the periodic table, and a tilted/flat arrangement to favor a metal-carbon π bond with transition metals to the left of iron in the periodic table. One can therefore envision that the metal-carbon contact resistance may be systematically varied by the deliberate selection of transition-metal substrates.

These theoretical insights provide a fundamental basis on which nanoparticle charge-transfer dynamics may be further manipulated. In fact, reports of transition-metal nanoparticles protected by metal-carbon covalent bonds have recently started to appear, allowing nanoparticle optoelectronic properties to be examined and compared within the context of metal-ligand interfacial contacts. Of these, the enhanced metal-ligand bonding interactions as a consequence of metal-carbon covalent bonds are anticipated to lead to extended spilling of the nanoparticle core electrons into the organic protecting matrix, and hence enhanced interparticle charge transfer (75–80).

In a recent study, Mirkhalaf et al. (75) used aryl diazonium derivatives as both the phase-transfer reagents and precursors for nanoparticle surface stabilization to prepare platinum (3 ± 1-nm diameter) and gold (8.0 ± 0.8-nm diameter) nanoparticles capped with metal-carbon covalent linkages (**Figure 10**) (75). Surface-enhanced Raman spectroscopic measurements (79) showed that the Pt-C vibrational band likely appeared within the range 410–420 cm^{-1}. The procedure was also adopted to prepare palladium (76), ruthenium (80), and titanium (77) nanoparticles capped with various aryl derivatives by metal-carbon bonds. The resulting nanoparticles exhibited electronic

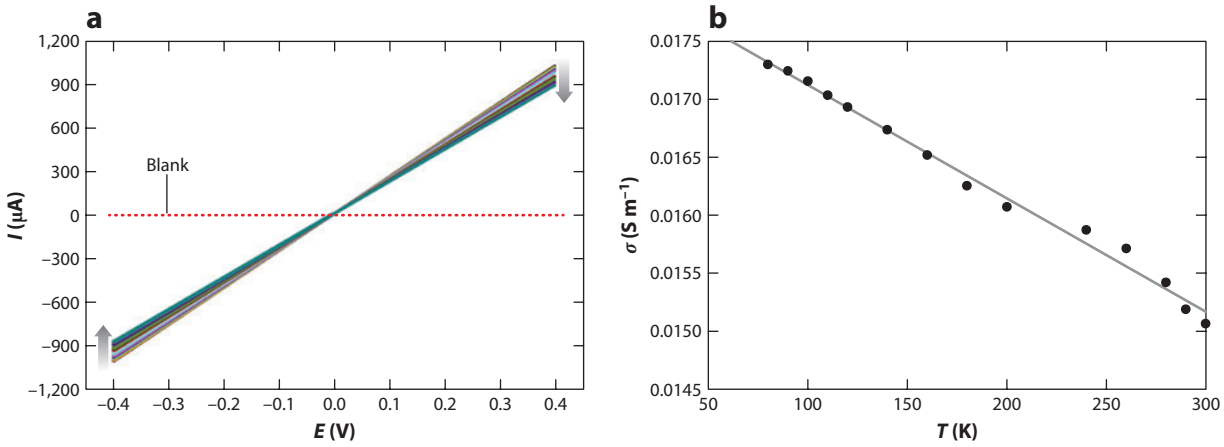

Figure 11

(*a*) Current-potential profiles of a biphenyl-capped palladium nanoparticle dropcast thick film at various temperatures. The potential scan rate is 20 mV s^{-1}. The red dotted line represents control measurements with the same blank electrode. (*b*) Variation of the ensemble conductivity with temperature. Figure reproduced with permission from Reference 76, copyright (2008) Royal Society of Chemistry.

conductivity that was markedly greater than that of the mercapto-passivated counterparts. For instance, biphenyl-capped palladium (Pd-BP) nanoparticles were prepared using 4-biphenyl diazonium as the precursor, with an average core diameter of 3.6 ± 0.8 nm, and the electronic conductivity was measured at controlled temperatures at which the nanoparticles were deposited onto an interdigitated array electrode. The I-V profiles exhibited a rather interesting dependence on temperature. **Figure 11*a*** shows the I-V curves of the Pd-BP nanoparticles within the temperature range 80–300 K. The I-V responses exhibit a linear (ohmic) character within the entire temperature range under study, suggesting efficient interparticle charge transfer. This is not surprising, considering the short and aromatic capping layer. As compared to control measurements with the same blank electrode (current of the order of picoamperes), the currents of the particle solid films are significantly greater, of the order of milliamperes, even at a potential bias of only ±0.4 V. More importantly, the currents are found to decrease with increasing temperature (80 K to 320 K), a behavior actually anticipated for metallic materials (81). From the slope of the I-V curves, one can calculate the conductivity of the particle solid films, which is of the order of 10^{-2} S m^{-1} (**Figure 11*b***). This is about nine orders of magnitude smaller than that of bulk palladium [approximately 0.93×10^7 S m^{-1} at room temperature (81)], which can be ascribed to the metal-organic nanocomposite nature of the particles. Additionally, the particle conductivity decreases (almost linearly) with temperature in the range 80–300 K (**Figure 11*b***). Although the decrease is less dramatic than that of the bulk metal, the observation deviates significantly from previous studies of metal nanoparticles protected with arylthiol derivatives in which the conductivity is generally found to increase with increasing temperature (73, 82–85); namely, the particle ensembles behave as semiconductor materials.

As the average core diameter of Pd-BP nanoparticles is ∼3 nm, the particle cores will behave similarly to bulk palladium. Thus the ensemble conductivity is anticipated to be mainly determined by the palladium-ligand contact and the ligand matrix itself. Yet, as mentioned above, palladium has extensively been used as the metal of choice to create contacts with carbon nanotubes because of strong Pd-C bonding interactions and low contact resistance (60–62). Furthermore, the π-π stacking as a result of ligand intercalations between adjacent particles in the solid films may serve

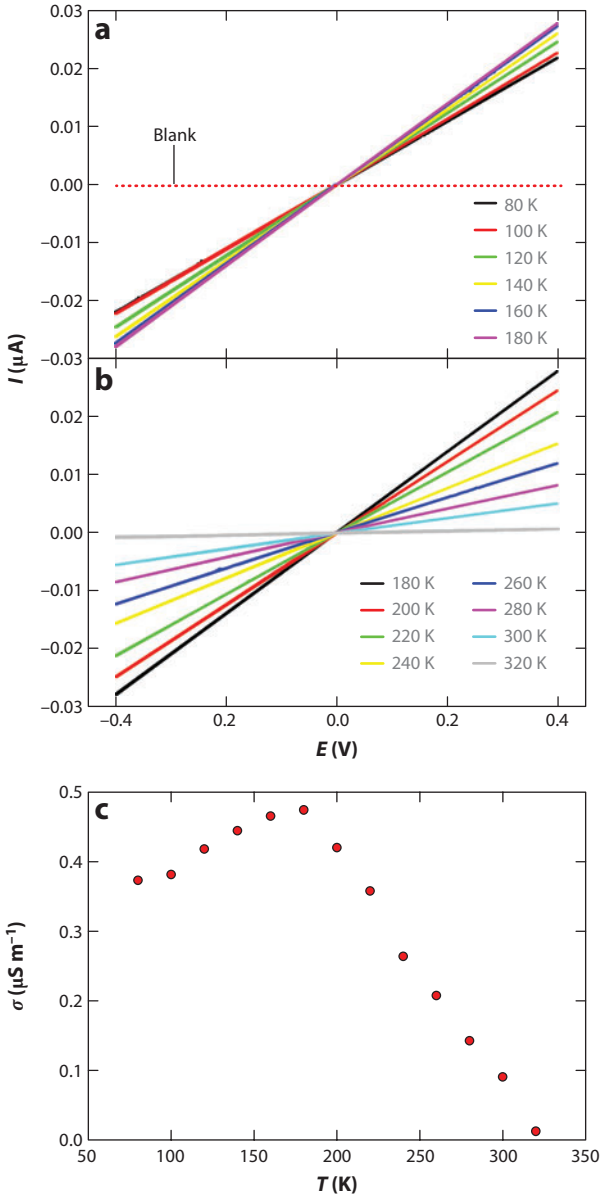

Figure 12

(*a*, *b*) Current-potential profiles of a decylphenyl-stabilized palladium nanoparticle dropcast thick film at various temperatures. The potential scan rate is 20 mV s^{-1}. The red dotted line represents control measurements with the same blank electrode. (*c*) Variation of the ensemble conductivity with temperature. Figure reproduced with permission from Reference 76, copyright (2008) Royal Society of Chemistry.

as an effective pathway for interparticle charge transfer (86). Hence it is most probable that the combination of these factors gives rise to the metal-like conductivity properties of Pd-BP particle solids.

The introduction of a saturated spacer into the capping ligands causes the resulting particles to exhibit drastic differences in I-V measurements. **Figure 12*a*,*b*** depicts the I-V data of decylphenyl-

stabilized palladium (Pd-DP) particles prepared in a similar fashion. The linear I-V profiles can also be seen within the entire temperature range of 80–320 K (**Figure 12**), but the magnitude of the currents (of the order of tens of nanoamperes) is substantially smaller than that observed with Pd-BP particles (**Figure 11**), although it is still significantly larger than that of the background currents. This can be ascribed to the long decyl spacer that impedes interparticle charge transfer.

In contrast to the Pd-BP particles, which exhibit a monotonic decrease in ensemble conductivity with increasing temperature (**Figure 11**), the behaviors of Pd-DP particles are somewhat more complicated. From **Figure 12*a***, one can see that the current first increases with increasing temperature from 80 to 180 K, exhibiting semiconductor characters, yet with a further increase in temperature (from 180 to 320 K), the current actually starts to decrease (**Figure 12*b***), akin to that observed in **Figure 11** in which the particle films behave instead like metallic materials. **Figure 12*c*** summarizes the ensemble conductivity with temperature and clearly depicts a transition temperature at approximately 180 K at which the interparticle charge transfer evolves from semiconductor to metallic behaviors.

These unique charge-transfer behaviors were also observed with ruthenium (80) and titanium (77) nanoparticles capped by similar aryl fragments. In sharp contrast, for (even slightly larger) palladium nanoparticles passivated by mercapto derivatives, the corresponding I-V profiles exhibited only semiconducting characters within the same range of temperature (87).

However, such a semiconductor-metal transition is not limited to nanoparticles capped with metal-carbon bonds. In a previous study of the resistivity of monolayers of much larger silver nanoparticles (7.8-nm diameter) passivated by octanethiolates or decanethiolates (88), the films exhibit a metal-like resistance at temperatures above 200 K, whereas at lower temperatures (60 to 200 K), the films behave as a semiconductor. In another study, Snow & Wohltjen (84) measured the conductance of solid films of dodecanethiolate-stabilized gold nanoparticles of varied sizes. For particles with a core diameter less than 5.0 nm, the authors observed only a semiconductor-like temperature dependence of the ensemble conductivity within the temperature range 190–300 K. For larger particles (core diameters of approximately 6.0 nm and 7.2 nm), the ensemble conductivity evolved from semiconducting to metallic behaviors with increasing temperature, and the transition temperature decreased with increasing particle core size, from 260 K (6.0 nm) to 240 K (7.2 nm). More recently, Murray and colleagues (89) reported that temperature-induced core motion could also lead to a drastic enhancement of the ensemble conductivity as a consequence of the thermal modulation of interparticle separations.

Taken together, the above observations can be rationalized by Mott's model for the metal-insulator transition (90). According to this model, a compressed lattice of hydrogen atoms is anticipated to exhibit metallic behaviors when the interatomic distance approaches $\sim 4.5a_0$, where a_0 is the Bohr radius. By approximating nanoparticles as artificial atoms, one obtains $a_0 : \frac{\hbar}{\sqrt{2m^*\phi}}$, where m^* is the effective mass of the electrons, ϕ is the barrier height, and $\hbar$ is Planck's constant. Thus the transition of the conductance of a nanoparticle ensemble into the metallic domain only occurs when the interparticle charge transfer is sufficiently enhanced. This can be achieved by increasing the particle core size (thus lowering the coulombic barrier for interparticle charge transfer), decreasing the particle-ligand contact resistance (hence enhancing electronic spilling beyond the metal cores), and raising the ensemble temperature (by virtue of thermal activation and core thermal motions). Thus, whereas the above-mentioned Pd-DP particles are substantially smaller than the Au-SR (84) and Ag-SR (88) particles that exhibit similar semiconductor-metal transitions with increasing temperature, the Pd-DP particles benefit from the strong Pd-C bonding and hence the markedly reduced interfacial contact resistance that offset the core size effects.

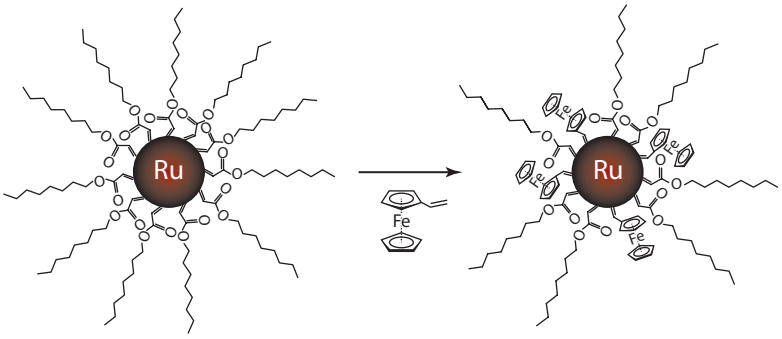

Figure 13

Olefin metathesis reaction of carbene-functionalized nanoparticles. Figure reproduced with permission from Reference 93, copyright (2008) American Chemical Society.

3.2. Metal-Carbene Bonds

More complicated metal-ligand interfacial bonding interactions have also been achieved using diazo ligands as the precursors, which are self-assembled onto metal nanoparticle surfaces forming metal-carbene π bonds and concurrently releasing nitrogen (91, 92). The conjugated interfacial bonds endow two unique properties to the nanoparticles. The first is that the nanoparticles may be further functionalized by olefin metathesis reactions with vinyl derivatives, and the other is that extended conjugation may emerge between particle-bound functional moieties, for which effective intraparticle charge delocalization may occur, leading to the appearance of unprecedented optical and electronic properties of the nanoparticle materials. This is drastically different from those described in Section 3.1 with metal-carbon single bonds. For instance, nanoparticle-mediated intervalence transfer was reported with ferrocene moieties that were attached onto the ruthenium nanoparticle surface by ruthenium-carbene π bonds using vinylferrocene as the illustrating example, Ru = CH-Fc (**Figure 13**) (93). The resulting particles exhibited two pairs of voltammetric waves with a potential spacing of approximately 200 mV (**Figure 14**), arising from the redox reactions of particle-bound ferrocene, $Fc^+ + e \leftrightarrow Fc$, and a rather intense absorption peak in the near-infrared range (~1,930 nm) at mixed valence. Both features were consistent with those of dimeric ferrocene with a conjugated chemical bridge and suggested class II characteristics of the intraparticle intervalence transfer that mainly arose from through-bond interactions between the metal centers (94). Quantum calculations based on DFT showed that the nanoparticle core electrons served as conducting band states for the effective charge delocalization between particle-bound ferrocene moieties. In contrast, when the nanoparticles were functionalized with allylferrocene in which an sp^3 carbon was inserted into the interfacial bridge (Ru = CH-CH_2-Fc), the electronic communication diminished drastically, leading to the appearance of only one pair of voltammetric waves, analogous to monomeric ferrocene (95). Similar behaviors were observed when the ferrocene moieties were bound onto a (macroscopic) metal electrode surface by similar ruthenium-carbene π bonds (96). These studies provide a first direct verification of Hush's (97) hypothesis made more than four decades ago that effective electronic communication might take place when redox-active moieties are anchored onto an electrode surface by a conjugated linker.

When fluorophores [e.g., pyrene (98) and anthracene (99)] are bound onto the nanoparticle surface by similarly conjugated metal-ligand bonds, the nanoparticles exhibit optical properties that are consistent with those of their dimeric derivatives. For instance, in a recent study, we prepared ruthenium nanoparticles functionalized with pyrene moieties by olefin metathesis re-

Intervalence charge transfer: an electron transfer (thermal or photoinduced) process between two identical metal centers at different valence states

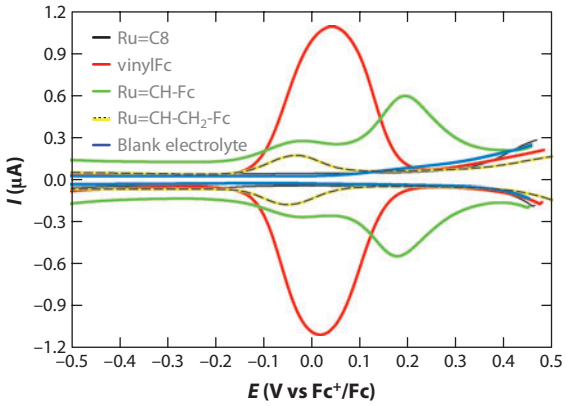

Figure 14

Square-wave voltammograms of vinylferrocene (vinylFc) monomers (0.1 mM, *red line*), Ru = C8 (4.7 mg mL^{-1}, *black line*), Ru = CH-Fc (5 mg mL^{-1}, *green line*), and Ru = CH-CH_2-Fc (2 mg mL^{-1}, *yellow-black dashed line*) particles in DMF containing 0.1-M TBAP. Also shown is the square-wave voltammogram acquired after the electrode was removed from the Ru = CH-Fc particle solution, rinsed with DMF, and then immersed in a blank electrolyte (*blue*). Experimental conditions are as follows: a gold disk electrode area 0.3 mm^2, increment of potential 4 mV, amplitude 25 mV, and frequency 15 Hz. Figure reproduced with permission from Reference 93, copyright (2008) American Chemical Society.

actions of carbene-stabilized nanoparticles with 1-vinylpyrene and 1-allylpyrene (referred to as Ru = VPy and Ru = APy, respectively) (98). In fluorescence measurements, Ru = VPy nanoparticles exhibited two prominent emission bands at 392 nm and 490 nm, similar to those of (*E*)-1,2-di(pyren-1-yl)ethene, suggesting that the particle-bound pyrene moieties behave equivalently to pyrene dimers with a conjugated linker by virtue of the ruthenium-carbene π bonds. In sharp contrast, Ru = APy nanoparticles displayed only a single emission peak at 392 nm, consistent with monomeric pyrene derivatives of 1-vinylpyrene and 1-allylpyrene. This again implies that the intraparticle extended conjugation was effectively turned off by the insertion of an sp^3 carbon into the chemical linker that bound the pyrene moieties onto the nanoparticles.

3.3. Metal-Alkynide Bonds

Recently we also functionalized ruthenium nanoparticles with 1-octynyl fragments by the formation of Ru-C≡ interfacial bonds (**Figure 15**) (100). Experimentally, 1-octyne first reacted with *n*-butyl lithium to produce 1-octynide lithium, which was then added into a solution of $RuCl_3$.

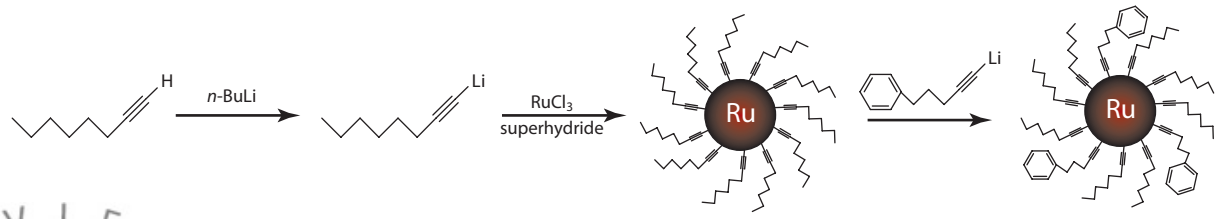

Figure 15

Schematic of the preparation of alkynide-protected nanoparticles. Figure reproduced with permission from Reference 100, copyright (2010) American Chemical Society.

Reduction by superhydride led to the production of octynide-protected ruthenium nanoparticles. Transmission electron microscopic measurements showed that the resulting particles exhibited an average core diameter of 2.55 ± 0.15 nm with well-defined ruthenium crystalline lattice fringes. Because of the formation of Ru-C≡ interfacial bonds, the C≡C vibrational stretch in Fourier transform infrared (FTIR) measurements red-shifted to 1,936 cm^{-1} from 2,119 cm^{-1} that was observed for monomeric 1-octyne. Interestingly, the nanoparticles underwent ligand exchange reactions with alkynyl lithium (e.g., 5-phenyl-1-pentynyl lithium) for further surface functionalization (**Figure 15**), as manifested in FTIR as well as ^{1}H and ^{13}C NMR measurements. Optically, whereas ultraviolet-visible absorption measurements exhibited only a featureless profile, the ruthenium nanoparticles displayed apparent photoluminescence with an emission peak at 428 nm, which was accounted for by intraparticle charge delocalization as a consequence of the strong Ru-C≡ interfacial bonds and the conducting ruthenium metal cores such that the particle-bound C≡C moieties behaved analogously to diacetylene (-C≡C-C≡C-) derivatives. The impacts of the interfacial bonding interactions on intraparticle charge delocalization were further illustrated by ruthenium nanoparticles functionalized with a mixed monolayer of both octynyl and ethynylferrocene ligands. At a ferrocene surface coverage of approximately 13%, electrochemical measurements depicted two pairs of voltammetric peaks with a potential spacing of 265 mV. A new near-infrared absorption band centered at approximately 1,687 nm also started to emerge with the addition of nitrosonium tetrafluoroborate ($NOBF_4$) as the oxidizing reagent, and the peak intensity exhibited a volcano-shape dependence on the amount of $NOBF_4$ added. These observations strongly suggest an effective intervalence charge transfer between the particle-bound ferrocene groups at mixed valence, analogous to the observation of ferrocene moieties bound onto the particle surface by ruthenium-carbene π bonds (93). Yet the larger potential spacing between the two voltammetric peaks and the higher energy of the near-infrared absorption peak indicate that the conjugation between the particle-bound ferrocenyl moieties appeared to be stronger with the Ru-C≡ bonds than with the Ru = C bonds.

3.4. Ruthenium-Vinylidene Bonds

In a more recent study, Kang et al (101) stabilized ruthenium nanoparticles by the self-assembly of 1-alkynes onto the bare ruthenium colloid surface (**Figure 16**). The formation of a ruthenium-vinylidene (Ru = C = CH-R) interfacial bonding linkage was confirmed by the specific reactivity of the nanoparticles with imine derivatives forming a heterocyclic complex at the metal-ligand interface, as manifested in ^{1}H and ^{13}C NMR, photoluminescence, and electrochemical measurements in which a ferrocenyl imine was used as the labeling probe. Notably, the resulting nanoparticles could also undergo olefin metathesis reactions with vinyl-terminated molecules, as exemplified by the functionalization of the nanoparticles with 1-vinylpyrene (98). In sharp contrast, no reactivity was observed with 1-dodecynide-stabilized ruthenium nanoparticles with either imine or vinyl derivatives because these (deprotonated) nanoparticles were stabilized instead by the formation of a Ru-C≡ dπ bond at the metal-ligand interface.

With this unique interfacial bond, the nanoparticles exhibit interesting electronic conductivity properties with linear I-V curves within the potential range of −0.8 V to +0.8 V at varied temperatures (200–300 K) (102). The ohmic characters were partly ascribed to the spilling of core electrons into the organic capping layer that facilitated interparticle charge transfer (vide ante; see Section 3.1). Furthermore, studies of the nanoparticle electronic conductivity showed that the coupling coefficient (β) was approximately 0.31 $Å^{-1}$ for nanoparticles stabilized by short-chain alkynes (1-hexyne, 1-octyne, and 1-decyne) and 1.44 $Å^{-1}$ for those with long-chain alkynes, such as 1-dodecyne, 1-tetradecyne, and 1-hexadecyne. This may be accounted for by the relative

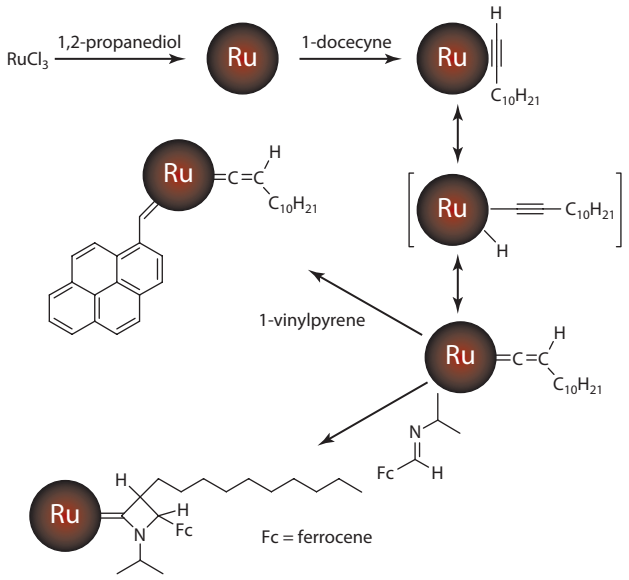

Figure 16

Synthesis and functionalization of alkyne-functionalized nanoparticles. Figure reproduced with permission from Reference 101, copyright (2012) American Chemical Society.

contributions of the conjugated metal-ligand interfacial bonding interactions versus the saturated aliphatic backbones of the alkyne ligands to the control of interparticle charge transfer.

3.5. Manipulation of Intraparticle Charge Delocalization

As mentioned above, intraparticle charge delocalization is facilitated by conjugated metal-ligand bonding interactions as well as the conducting metal cores (93). Thus the manipulation of the core valence state is anticipated to impact the electronic communication between nanoparticle-bound functional moieties. Using 1-octynide-stabilized ruthenium nanoparticles as the illustrating example, Kang et al. (103) demonstrated that intraparticle charge delocalization can be readily manipulated by the nanoparticle charge state, which was achieved by chemical reduction or oxidation. This is in sharp contrast to earlier work with gold nanoparticles passivated by thiol derivatives in which the impacts of the depletion or injection of core free electrons were essentially confined to metallic cores (104). For instance, for nanoparticles with a net gain (loss) of 0.6 electron per particle by $NaBH_4$ reduction [$Ce(SO_4)_2$ oxidation], the bonding order of the particle-bound C≡C moieties exhibited an apparent decrease (enhancement), as manifested in FTIR and X-ray photoelectron spectroscopy measurements. This suggests that the extended conjugation between the particle-bound C≡C moieties became strengthened (weakened) when the nanoparticles were charged (discharged), which may result from the nanoparticle metallic cores serving as the conducting media to facilitate intraparticle charge delocalization. As a result, the nanoparticle photoluminescence characteristics vary accordingly. Whereas the peak position of the emission profiles exhibits only a slight variation, the intensity of the reduced nanoparticles was markedly enhanced and that of the oxidized nanoparticles exhibited an apparent suppression, in comparison to the as-prepared nanoparticles. These results demonstrate that nanoparticle optoelectronic properties may be further manipulated by the nanoparticle charge state, by taking advantage of the molecular capacitor characters of the particles as well as the strong metal-ligand interfacial bonding interactions.

Further studies show that electrostatic polarization of the nanoparticle core electrons by the selective binding of metal cations to the particle-bound functional moieties also leads to an apparent variation of the nanoparticle-mediated electronic communication (105, 106). This behavior may be exploited for chemical sensing applications.

4. SUMMARY AND PERSPECTIVES

In this review article, we highlight some recent studies on the fundamental significance of metal-organic contacts in the manipulation of the dynamics of interfacial charge transfer, a critical process in molecular and nanoscale electronics. Whereas most studies have been confined to interfaces with metal-thiolate bonds, recent studies have shown that metal-carbon covalent bonds may also be formed at the metal-ligand interface, which exhibit markedly reduced interfacial resistance in comparison with the corresponding metal-thiolate counterparts. As such, the energetic barrier in charge transport across molecular junctions may be reduced significantly. Furthermore, for organically capped nanoparticles, the conjugated nature of the interfacial linkages leads to effective intraparticle charge delocalization and hence enhanced charge transport between neighboring nanoparticles.

Within this context, one may ask what other metal-nonmetal bonds are possible in the fabrication of molecular junctions or functionalization of nanoparticles. We note that in addition to metal-carbon bonds, a wide variety of metal-nonmetal bonds has been rather extensively observed in organometallic chemistry, such as metal-nitrogen and metal-silicon bonds. Of these, metal-nitrene (M = N) bonds have been proposed or recognized in a variety of organometallic complexes that are involved in bond-activation reactions (e.g., C-H bond activation, nitrene-exchange or nitrene-transfer reactions), in which the unique reactivity is attributed to the high polarizability of the M = N bonds (107–109). It is generally believed that the nitrene group is stabilized by the $d\pi$ (metal) $\rightarrow$ $p\pi$ (nitrene) back-bonding interactions that involve both σ and π components (110, 111). In addition, metal-silicon bonds have been formed with a variety of transition metals (112–115). An understanding of the chemical nature and reactivity of the metal-silicon bonds (116–118) is anticipated to shed light on the formation and manipulation of the energetic barrier for interfacial charge transport in silicon-based semiconductor devices, for which metal-silicon contacts are an essential component (119).

Yet it remains a challenge to develop effective procedures to create reliable metal-nitrogen or metal-silicon bonds at molecular junctions or on metal nanoparticle surfaces (120). This is limited primarily by the lack of appropriate organic functional moieties. Thus the rational design and synthesis of unique organic ligands represent critical first steps in unraveling the mechanistic insights of the impacts of these interfacial bonding contacts on the charge-transport dynamics involved. It is envisaged that the rich reactivity of these metal-ligand bonds, as manifested in diverse organometallic complexes, may be exploited as a unique platform for further and more deliberate functionalization and engineering of molecular and nanoscale electronic assemblies and devices.

SUMMARY POINTS

1. Charge transfer through bonded contacts is more efficient than that through nonbonded contacts, suggesting that the energetic barrier for through-bond transfer is lower than that for through-space transfer.
2. Interfacial contact resistance may be diminished drastically with metal-carbon covalent linkages, as compared with the metal-thiolate ones, for which the work functions of the metal substrates also play an important role.

3. For conjugated metal-carbon linkages, effective electronic communication may occur between functional moieties bound onto metal electrode or nanoparticle surfaces.
4. More diverse metal-ligand interfacial bonding interactions may be achieved by a rational design and synthesis of unique functional ligands.

DISCLOSURE STATEMENT

The authors are not aware of any affiliations, memberships, funding, or financial holdings that might be perceived as affecting the objectivity of this review.

ACKNOWLEDGMENTS

The authors acknowledge financial support from the US National Science Foundation (CHE-1012258, DMR-0807049, and CBET-1258839), the National Natural Science Foundation of China (NSFDYS-5092505 and 51002089), the Innovation Research Group (IRG-51021062), the Natural Science Funds for Distinguished Young Scholars of Shandong Province (JQ201117), the Program of Introducing Talents of Disciplines to Universities in China (the 111 Program b06015), and the American Chemical Society Petroleum Research Funds (49137-ND10).

LITERATURE CITED

1. Presents the first concept on electronic devices based on simple organic molecules.

1. **Aviram A, Ratner MA. 1974. Molecular rectifiers. *Chem. Phys. Lett.* 29:277–83**
2. Flood AH, Ramirez RJA, Deng WQ, Muller RP, Goddard WA, Stoddart JF. 2004. Meccano on the nanoscale: a blueprint for making some of the world's tiniest machines. *Aust. J. Chem.* 57:301–22
3. Vuillaume D, Lenfant S, Guerin D, Delerue C, Petit C, Salace G. 2006. Electronic properties of organic monolayers and molecular devices. *Pramana J. Phys.* 67:17–32
4. Kula M, Jiang J, Luo Y. 2008. A molecular view on electron transport in molecular electronic devices. *J. Comput. Theoret. Nanosci.* 5:401–21
5. Bergren AJ, McCreery RL. 2011. Analytical chemistry in molecular electronics. *Annu. Rev. Anal. Chem.* 4:173–95
6. Zhu XY. 2004. Electronic structure and electron dynamics at molecule-metal interfaces: implications for molecule-based electronics. *Surf. Sci. Rep.* 56:1–83
7. Porter LM, Davis RF. 1995. A critical review of ohmic and rectifying contacts for silicon carbide. *Mater. Sci. Eng. B* 34:83–105
8. Bozack MJ. 1997. Surface studies on SiC as related to contacts. *Phys. Status Solidi B* 202:549–80
9. Murakami M, Koide Y. 1998. Ohmic contacts for compound semiconductors. *Crit. Rev. Solid State* 23:1–60
10. Evans DA, Roberts OR, Williams GT, Vearey-Roberts AR, Bain F, et al. 2009. Diamond-metal contacts: interface barriers and real-time characterization. *J. Phys. Condens. Matter* 21:364223
11. Templeton AC, Wuelfing MP, Murray RW. 2000. Monolayer protected cluster molecules. *Acc. Chem. Res.* 33:27–36
12. Whetten RL, Shafigullin MN, Khoury JT, Schaaff TG, Vezmar I, et al. 1999. Crystal structures of molecular gold nanocrystal arrays. *Acc. Chem. Res.* 32:397–406
13. Templeton AC, Hostetler MJ, Warmoth EK, Chen SW, Hartshorn CM, et al. 1998. Gateway reactions to diverse, polyfunctional monolayer-protected gold clusters. *J. Am. Chem. Soc.* 120:4845–49
14. Brust M, Bethell D, Kiely CJ, Schiffrin DJ. 1998. Self-assembled gold nanoparticle thin films with nonmetallic optical and electronic properties. *Langmuir* 14:5425–29
15. Collier CP, Vossmeyer T, Heath JR. 1998. Nanocrystal superlattices. *Annu. Rev. Phys. Chem.* 49:371–404

16. Shenhar R, Rotello VM. 2003. Nanoparticles: scaffolds and building blocks. *Acc. Chem. Res.* 36:549–61
17. Likharev KK. 1988. Correlated discrete transfer of single electrons in ultrasmall tunnel junctions. *IBM J. Res. Dev.* 32:144–58
18. Jiang P, Liu ZF, Cai SM. 1999. In situ CdS nanocluster formation on scanning tunneling microscopy tips for reliable single-electron tunneling at room temperature. *Appl. Phys. Lett.* 75:3023–25
19. Hanna AE, Tinkham M. 1991. Variation of the coulomb staircase in a two-junction system by fractional electron charge. *Phys. Rev. B* 44:5919–22
20. Chen SW. 2004. Chemical manipulations of nanoscale electron transfers. *J. Electroanal. Chem.* 574:153–65
21. **Murray RW. 2008. Nanoelectrochemistry: metal nanoparticles, nanoelectrodes, and nanopores. *Chem. Rev.* 108:2688–720**
22. Su B, Girault HH. 2005. Absolute standard redox potential of monolayer-protected gold nanoclusters. *J. Phys. Chem. B* 109:11427–31
23. Remacle F. 2000. On electronic properties of assemblies of quantum nanodots. *J. Phys. Chem. A* 104:4739–47
24. Beverly KC, Sampaio JF, Heath JR. 2002. Effects of size dispersion disorder on the charge transport in self-assembled 2-D Ag nanoparticle arrays. *J. Phys. Chem. B* 106:2131–35
25. Andres RP, Bein T, Dorogi M, Feng S, Henderson JI, et al. 1996. "Coulomb staircase" at room temperature in a self-assembled molecular nanostructure. *Science* 272:1323–25
26. Tran TB, Beloborodov IS, Hu JS, Lin XM, Rosenbaum TF, Jaeger HM. 2008. Sequential tunneling and inelastic cotunneling in nanoparticle arrays. *Phys. Rev. B* 78:075437
27. Chen SW, Templeton AC, Murray RW. 2000. Monolayer-protected cluster growth dynamics. *Langmuir* 16:3543–48
28. Wang G, Kim TW, Jang YH, Lee T. 2008. Effects of metal-molecule contact and molecular structure on molecular electronic conduction in nonresonant tunneling regime: alkyl versus conjugated molecules. *J. Phys. Chem. C* 112:13010–16
29. Reed MA, Zhou C, Deshpande MR, Muller CJ, Burgin TP, et al. 1998. The electrical measurement of molecular junctions. *Ann. NY Acad. Sci.* 852:133–44
30. **Chen F, Hihath J, Huang ZF, Li XL, Tao NJ. 2007. Measurement of single-molecule conductance. *Annu. Rev. Phys. Chem.* 58:535–64**
31. Calame M. 2010. Molecular junctions: from tunneling to function. *Chimia* 64:391–97
32. Nichols RJ, Haiss W, Higgins SJ, Leary E, Martin S, Bethell D. 2010. The experimental determination of the conductance of single molecules. *Phys. Chem. Chem. Phys.* 12:2801–15
33. Song H, Reed MA, Lee T. 2011. Single molecule electronic devices. *Adv. Mater.* 23:1583–608
34. Ward DR, Scott GD, Keane ZK, Halas NJ, Natelson D. 2008. Electronic and optical properties of electromigrated molecular junctions. *J. Phys. Condens. Matter* 20:374118
35. Hybertsen MS, Venkataraman L, Klare JE, Whalley CA, Steigerwald ML, Nuckolls C. 2008. Amine-linked single-molecule circuits: systematic trends across molecular families. *J. Phys. Condens. Matter* 20:374115
36. Watanabe M. 2005. Technologies for the fabrication of nanoscale superconducting circuits. *Mod. Phys. Lett. B* 19:405–24
37. Troadec C, Jie D, Kunardi L, O'Shea SJ, Chandrasekhar N. 2004. Metal-organic interfaces at the nanoscale. *Nanotechnology* 15:1818–24
38. Heath JR. 2009. Molecular electronics. *Annu. Rev. Mater. Res.* 39:1–23
39. Cui XD, Primak A, Zarate X, Tomfohr J, Sankey OF, et al. 2001. Reproducible measurement of single-molecule conductivity. *Science* 294:571–74
40. Engelkes VB, Beebe JM, Frisbie CD. 2004. Length-dependent transport in molecular junctions based on SAMs of alkanethiols and alkanedithiols: effect of metal work function and applied bias on tunneling efficiency and contact resistance. *J. Am. Chem. Soc.* 126:14287–96
41. Simmons JG. 1963. Generalized formula for electric tunnel effect between similar electrodes separated by a thin insulating film. *J. Appl. Phys.* 34:1793–803
42. Joachim C, Magoga M. 2002. The effective mass of an electron when tunneling through a molecular wire. *Chem. Phys.* 281:347–52

21. Comprehensively reviews the synthesis, functionalization, and applications of stable organically capped nanoparticles.

30. Reviews the methods to the formation of single-molecule junctions and their charge-transport characteristics.

43. Lee T, Wang WY, Klemic JF, Zhang JJ, Su J, Reed MA. 2004. Comparison of electronic transport characterization methods for alkanethiol self-assembled monolayers. *J. Phys. Chem. B* 108:8742–50
44. Wang WY, Lee T, Reed MA. 2003. Mechanism of electron conduction in self-assembled alkanethiol monolayer devices. *Phys. Rev. B* 68:035416
45. Tomfohr J, Sankey OF. 2004. Theoretical analysis of electron transport through organic molecules. *J. Chem. Phys.* 120:1542–54
46. York RL, Nacionales D, Slowinski K. 2005. Electrical resistivity of monolayers and bilayers of alkanethiols in tunnel junction with gate electrode. *Chem. Phys.* 319:235–42
47. York RL, Nguyen PT, Slowinski K. 2003. Long-range electron transfer through monolayers and bilayers of alkanethiols in electrochemically controlled Hg-Hg tunneling junctions. *J. Am. Chem. Soc.* 125:5948–53
48. Holmlin RE, Ismagilov RF, Haag R, Mujica V, Ratner MA, et al. 2001. Correlating electron transport and molecular structure in organic thin films. *Angew. Chem. Int. Ed. Engl.* 40:2316–20
49. Ulman A. 1996. Formation and structure of self-assembled monolayers. *Chem. Rev.* 96:1533–54

50. Directly demonstates that metal-carbon covalent linkages exhibit markedly enhanced charge transport as compared to those based on metal-thiolate bonds.

50. Cheng ZL, Skouta R, Vazquez H, Widawsky JR, Schneebeli S, et al. 2011. In situ formation of highly conducting covalent Au-C contacts for single-molecule junctions. *Nat. Nanotechnol.* 6:353–57

51. Chen WB, Widawsky JR, Vazquez H, Schneebeli ST, Hybertsen MS, et al. 2011. Highly conducting π-conjugated molecular junctions covalently bonded to gold electrodes. *J. Am. Chem. Soc.* 133:17160–63
52. Yaffe O, Scheres L, Segev L, Biller A, Ron I, et al. 2010. Hg/molecular monolayer-Si junctions: electrical interplay between monolayer properties and semiconductor doping density. *J. Phys. Chem. C* 114:10270–79
53. Chen ZH, Appenzeller J, Knoch J, Lin YM, Avouris P. 2005. The role of metal-nanotube contact in the performance of carbon nanotube field-effect transistors. *Nano Lett.* 5:1497–502
54. Nemec N, Tomanek D, Cuniberti G. 2006. Contact dependence of carrier injection in carbon nanotubes: an ab initio study. *Phys. Rev. Lett.* 96:076802
55. Buonocore F. 2010. First-principles investigation of the interaction of gold and palladium with armchair carbon nanotube. *Mol. Simul.* 36:729–35
56. Vitale V, Curioni A, Andreoni W. 2008. Metal-carbon nanotube contacts: the link between Schottky barrier and chemical bonding. *J. Am. Chem. Soc.* 130:5848–49
57. Luo J, Zhu J. 2006. Arrays of one-dimensional metal/silicon and metal/carbon nanotube heterojunctions. *Nanotechnology* 17:S262–70
58. Nihei M, Horibe M, Kawabata A, Awano Y. 2004. Simultaneous formation of multiwall carbon nanotubes and their end-bonded ohmic contacts to Ti electrodes for future ULSI interconnects. *Jpn. J. Appl. Phys.* 43:1856–59
59. Matsuda Y, Deng WQ, Goddard WA. 2010. Contact resistance for "end-contacted" metal-graphene and metal-nanotube interfaces from quantum mechanics. *J. Phys. Chem. C* 114:17845–50
60. Mann D, Javey A, Kong J, Wang Q, Dai HJ. 2003. Ballistic transport in metallic nanotubes with reliable Pd ohmic contacts. *Nano Lett.* 3:1541–44
61. Tarakeshwar P, Kim DM. 2005. Modulation of the electronic structure of semiconducting nanotubes resulting from different metal contacts. *J. Phys. Chem. B* 109:7601–4
62. Woo Y, Duesberg GS, Roth S. 2007. Reduced contact resistance between an individual single-walled carbon nanotube and a metal electrode by a local point annealing. *Nanotechnology* 18:095203
63. Nirmalraj PN, Boland JJ. 2010. Selective tuning and optimization of the contacts to metallic and semiconducting single-walled carbon nanotubes. *ACS Nano* 4:3801–6
64. Hsu A, Wang H, Kim KK, Kong J, Palacios T. 2011. Impact of graphene interface quality on contact resistance and RF device performance. *IEEE Electron. Device Lett.* 32:1008–10

65. Provides the first report of the preparation of stable organically capped nanoparticles.

65. Brust M, Walker M, Bethell D, Schiffrin DJ, Whyman R. 1994. Synthesis of thiol-derivatized gold nanoparticles in a two-phase liquid-liquid system. *J. Chem. Soc. Chem. Commun.* 1994:801–2

66. Chen SW, Murray RW. 1999. Arenethiolate monolayer-protected gold clusters. *Langmuir* 15:682–89
67. Vickers MS, Cookson J, Beer PD, Bishop PT, Thiebaut B. 2006. Dithiocarbamate ligand stabilised gold nanoparticles. *J. Mater. Chem.* 16:209–15

68. Tong MC, Chen W, Sun J, Ghosh D, Chen SW. 2006. Dithiocarbamate-capped silver nanoparticles. *J. Phys. Chem. B* 110:19238–42
69. Chen W, Ghosh D, Sun J, Tong MC, Deng FJ, Chen SW. 2007. Dithiocarbamate-protected ruthenium nanoparticles: synthesis, spectroscopy, electrochemistry and STM studies. *Electrochim. Acta* 53:1150–56
70. Terrill RH, Postlethwaite TA, Chen CH, Poon CD, Terzis A, et al. 1995. Monolayers in three dimensions: NMR, SAXS, thermal, and electron hopping studies of alkanethiol stabilized gold clusters. *J. Am. Chem. Soc.* 117:12537–48
71. Zamborini FP, Leopold MC, Hicks JF, Kulesza PJ, Malik MA, Murray RW. 2002. Electron hopping conductivity and vapor sensing properties of flexible network polymer films of metal nanoparticles. *J. Am. Chem. Soc.* 124:8958–64
72. Zamborini FP, Smart LE, Leopold MC, Murray RW. 2003. Distance-dependent electron hopping conductivity and nanoscale lithography of chemically-linked gold monolayer protected cluster films. *Anal. Chim. Acta* 496:3–16
73. Wuelfing WP, Murray RW. 2002. Electron hopping through films of arenethiolate monolayer-protected gold clusters. *J. Phys. Chem. B* 106:3139–45
74. Jiang DE, Sumpter BG, Dai S. 2006. Structure and bonding between an aryl group and metal surfaces. *J. Am. Chem. Soc.* 128:6030–31
75. Mirkhalaf F, Paprotny J, Schiffrin DJ. 2006. Synthesis of metal nanoparticles stabilized by metal-carbon bonds. *J. Am. Chem. Soc.* 128:7400–1
76. Ghosh D, Chen SW. 2008. Palladium nanoparticles passivated by metal-carbon covalent linkages. *J. Mater. Chem.* 18:755–62
77. Ghosh D, Pradhan S, Chen W, Chen SW. 2008. Titanium nanoparticles stabilized by Ti-C covalent bonds. *Chem. Mater.* 20:1248–50
78. Zhou ZY, Huang J, Kang XW, Song Y, Sun SG, Chen SW. 2012. Butylphenyl-functionalized Pt nanoparticles as CO-resistant electrocatalysts for formic acid oxidation. *Phys. Chem. Chem. Phys.* 14:1412–17
79. Zhou ZY, Kang XW, Song Y, Chen SW. 2012. Ligand-mediated electrocatalytic activity of Pt nanoparticles for oxygen reduction reactions. *J. Phys. Chem. C* 116:10592–98
80. Ghosh D, Chen SW. 2008. Solid-state electronic conductivity of ruthenium nanoparticles passivated by metal-carbon covalent bonds. *Chem. Phys. Lett.* 465:115–19
81. Lide DR. 2004. *CRC Handbook of Chemistry and Physics: A Ready-Reference Book of Chemical and Physical Data*. Boca Raton, FL: CRC
82. Clarke L, Wybourne MN, Brown LO, Hutchison JE, Yan M, et al. 1998. Room-temperature Coulomb-blockade-dominated transport in gold nanocluster structures. *Semicond. Sci. Technol.* 13:A111–14
83. Doty RC, Yu HB, Shih CK, Korgel BA. 2001. Temperature-dependent electron transport through silver nanocrystal superlattices. *J. Phys. Chem. B* 105:8291–96
84. Snow AW, Wohltjen H. 1998. Size-induced metal to semiconductor transition in a stabilized gold cluster ensemble. *Chem. Mater.* 10:947–50
85. Wang LY, Shi XJ, Kariuki NN, Schadt M, Wang GR, et al. 2007. Array of molecularly mediated thin film assemblies of nanoparticles: correlation of vapor sensing with interparticle spatial properties. *J. Am. Chem. Soc.* 129:2161–70
86. Pradhan S, Ghosh D, Xu LP, Chen SW. 2007. Interparticle charge transfer mediated by π-π stacking of aromatic moieties. *J. Am. Chem. Soc.* 129:10622–23
87. Chen SW. 2009. Electronic conductivity of nanoparticle solid thin films. In *Handbook of Electrochemical Nanotechnology*, ed. YH Lin, HS Nalwa, pp. 201–18. Los Angeles: Am. Sci.
88. Sampaio JF, Beverly KC, Heath JR. 2001. DC transport in self-assembled 2D layers of Ag nanoparticles. *J. Phys. Chem. B* 105:8797–800
89. Choi JP, Coble MM, Branham MR, DeSimone JM, Murray RW. 2007. Dynamics of CO_2-plasticized electron transport in Au nanoparticle films: opposing effects of tunneling distance and local site mobility. *J. Phys. Chem. C* 111:3778–85
90. Zabet-Khosousi A, Trudeau PE, Suganuma Y, Dhirani AA, Statt B. 2006. Metal to insulator transition in films of molecularly linked gold nanoparticles. *Phys. Rev. Lett.* 96:156403
91. Chen W, Davies JR, Ghosh D, Tong MC, Konopelski JP, Chen SW. 2006. Carbene-functionalized ruthenium nanoparticles. *Chem. Mater.* 18:5253–59

92. Tulevski GS, Myers MB, Hybertsen MS, Steigerwald ML, Nuckolls C. 2005. Formation of catalytic metal-molecule contacts. *Science* 309:591–94

93. Chen W, Chen SW, Ding FZ, Wang HB, Brown LE, Konopelski JP. 2008. Nanoparticle-mediated intervalence transfer. *J. Am. Chem. Soc.* 130:12156–62

94. Robin MB, Day P. 1967. Mixed-valence chemistry: a survey and classification. *Adv. Inorg. Chem. Radiochem.* 10:247–422

95. Nishihara H. 2001. Redox and optical properties of conjugated ferrocene oligomers. *Bull. Chem. Soc. Jpn.* 74:19–29

96. Chen W, Brown LE, Konopelski JP, Chen SW. 2009. Intervalence transfer of ferrocene moieties adsorbed on electrode surfaces by a conjugated linkage. *Chem. Phys. Lett.* 471:283–85

97. Hush NS. 1968. Homogeneous and heterogeneous optical and thermal electron transfer. *Electrochim. Acta* 13:1005–23

98. Chen W, Zuckerman NB, Lewis JW, Konopelski JP, Chen SW. 2009. Pyrene-functionalized ruthenium nanoparticles: novel fluorescence characteristics from intraparticle extended conjugation. *J. Phys. Chem. C* 113:16988–95

99. Chen W, Pradhan S, Chen SW. 2011. Photoluminescence and conductivity studies of anthracene-functionalized ruthenium nanoparticles. *Nanoscale* 3:2294–300

100. Chen W, Zuckerman NB, Kang XW, Ghosh D, Konopelski JP, Chen SW. 2010. Alkyne-protected ruthenium nanoparticles. *J. Phys. Chem. C* 114:18146–52

101. Kang XW, Zuckerman NB, Konopelski JP, Chen SW. 2012. Alkyne-functionalized ruthenium nanoparticles: ruthenium-vinylidene bonds at the metal-ligand interface. *J. Am. Chem. Soc.* 134:1412–15

102. Kang XW, Chen SW. 2012. Electronic conductivity of alkyne-capped ruthenium nanoparticles. *Nanoscale* 4:4183–89

103. Kang XW, Zuckerman NB, Konopelski JP, Chen SW. 2010. Alkyne-stabilized ruthenium nanoparticles: manipulation of intraparticle charge delocalization by nanoparticle charge states. *Angew. Chem. Int. Ed. Engl.* 49:9496–99

104. Templeton AC, Pietron JJ, Murray RW, Mulvaney P. 2000. Solvent refractive index and core charge influences on the surface plasmon absorbance of alkanethiolate monolayer-protected gold clusters. *J. Phys. Chem. B* 104:564–70

105. Kang XW, Chen W, Zuckerman NB, Konopelski JP, Chen SW. 2011. Intraparticle charge delocalization of carbene-functionalized ruthenium nanoparticles manipulated by selective ion binding. *Langmuir* 27:12636–41

106. Kang XW, Li X, Hewitt WM, Zuckerman NB, Konopelski JP, Chen SW. 2012. Manipulation of intraparticle charge delocalization by selective complexation of transition-metal ions with histidine moieties. *Anal. Chem.* 84:2025–30

107. Moiseev II, Stromnova TA, Vargaftik MN, Orlova ST, Chernysheva TV, Stolarov IP. 1999. Giant cluster catalysis: possible intermediacy of nitrene and carbene species. *Catal. Today* 51:595–602

108. Leung SKY, Tsui WM, Huang JS, Che CM, Liang JL, Zhu NY. 2005. Imido transfer from *bis*(imido)ruthenium(VI) porphyrins to hydrocarbons: effect of imido substituents, C-H bond dissociation energies, and RUVIN reduction potentials. *J. Am. Chem. Soc.* 127:16629–40

109. Heyduk AF, Zarkesh RA, Nguyen AI. 2011. Designing catalysts for nitrene transfer using early transition metals and redox-active ligands. *Inorg. Chem.* 50:9849–63

110. Brown GM, Callahan RW, Meyer TJ. 1975. Thermal and light-induced decomposition of azido(*bis*-2,2′-bipyridine) complexes of ruthenium(III). *Inorg. Chem.* 14:1915–21

111. Cundari TR. 1992. Transition-metal imido complexes. *J. Am. Chem. Soc.* 114:7879–88

112. Woo HG, Heyn RH, Tilley TD. 1992. Sigma-bond metathesis reactions for D(0) metal silicon bonds that produce zirconocene and hafnocene hydrosilyl complexes. *J. Am. Chem. Soc.* 114:5698–707

113. King WA, Marks TJ. 1995. Metal-silicon bonding energetics in organo-group-4 and organo-F-element complexes: implications for bonding and reactivity. *Inorg. Chim. Acta* 229:343–54

114. Wilfling M, Klinkhammer KW. 2010. Gold(I)-mediated silicon-silicon bond metathesis at room temperature. *Angew. Chem. Int. Ed. Engl.* 49:3219–23

93. Presents the first observation of electronic communication between nanoparticle-bound functional moieties through conjugated metal-ligand interfacial bonds.

94. Reviews organometallic complexes that exhibit intervalence transfer and their classification based on the extent of electronic interactions.

101. Identifies the formation of ruthenium-vinylidene interfacial bonds upon the self-assembly of 1-alkynes on ruthenium nanoparticle surfaces.

115. Filippou AC, Chernov O, Stumpf KW, Schnakenburg G. 2010. Metal-silicon triple bonds: the molybdenum silylidyne complex [$Cp(CO)_2Mo{\equiv}Si$-R]. *Angew. Chem. Int. Ed. Engl.* 49:3296–300
116. Lichtenberger DL, Raichaudhuri A. 1991. Electronic structure of transition-metal silicon bonds: valence photoelectron spectra of (η^5-C_5H_5)$Fe(CO)_2L$ complexes (L = $SiCl_3$, $Si(CH_3)_3$). *J. Am. Chem. Soc.* 113:2923–30
117. Hubler K, Hubler U, Roper WR, Schwerdtfeger P, Wright LJ. 1997. The nature of the metal-silicon bond in [$M(SiR^3)H$-$^3(PPh^3)^3$] (M = Ru, Os) and the crystal structure of [Os{Si(N-pyrrolyl)$_3$}$H_3(PPh_3)_3$]. *Chem. Eur. J.* 3:1608–16
118. Braunstein P, Knorr M. 1995. Reactivity of the metal-silicon bond in organometallic chemistry. *J. Organomet. Chem.* 500:21–38
119. Murarka SP. 1995. Silicide thin films and their applications in microelectronics. *Intermetallics* 3:173–86
120. Kang XW, Song Y, Chen SW. 2012. Nitrene-functionalized ruthenium nanoparticles. *J. Mater. Chem.* 22:19250–57